ACS APPLIED MATERIALS & INTERFACES

Research Article

www.acsami.org

Au/Polypyrrole@Fe_3O_4 Nanocomposites for MR/CT Dual-Modal Imaging Guided-Photothermal Therapy: An *in Vitro* Study

Wei Feng,[†,‡] Xiaojun Zhou,[‡] Wei Nie,[†,‡] Liang Chen,[†,‡] Kexin Qiu,[‡] Yanzhong Zhang,[†,‡] and Chuanglong He*[,†,‡]

[†]College of Chemistry, Chemical Engineering and Biotechnology, Donghua University, 2999 North Renmin Road, Shanghai 201620, China

[‡]State Key Laboratory for Modification of Chemical Fibers and Polymer Materials, Donghua University, Shanghai 201620, China

Supporting Information

ABSTRACT: Construction of multifunctional nanocomposites as theranostic platforms has received considerable biomedical attention. In this study, a triple-functional theranostic agent based on the cointegration of gold nanorods (Au NRs) and superparamagnetic iron oxide (Fe_3O_4) into polypyrrole was developed. Such a theranostic agent (referred to as Au/PPY@Fe_3O_4) not only exhibits strong magnetic property and high near-infrared (NIR) optical absorbance but also produces high contrast for magnetic resonance (MR) and X-ray computed tomography (CT) imaging. Importantly, under the irradiation of the NIR 808 nm laser at the power density of 2 W/cm^2 for 10 min, the temperature of the solution containing Au/PPY@Fe_3O_4 (1.4 mg/mL) increased by about 35 °C. Cell viability assay showed that these nanocomposites had low cytotoxicity. Furthermore, an *in vitro* photothermal treatment test demonstrates that the cancer cells can be efficiently killed by the photothermal effects of the Au/PPY@Fe_3O_4 nanocomposites. In summary, this study demonstrates that the highly versatile multifunctional Au/PPY@Fe_3O_4 nanocomposites have great potential in simultaneous multimodal imaging-guided cancer theranostic applications.

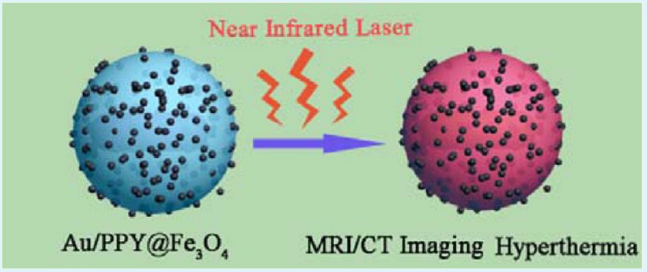

KEYWORDS: *Au/PPY@Fe_3O_4 nanocomposites, magnetic resonance imaging (MRI), X-ray computed tomography (CT), photothermal therapy, theranostics*

1. INTRODUCTION

The successful treatment of cancer remains a tremendous challenge for clinicians and researchers worldwide due to the complexities and variability involved in cancer progression. Conventional cancer therapies, comprising surgery, chemotherapy and radiotherapy, all encounter limitations such as incomplete resection of cancer tissue, high systemic toxicity, and multidrug resistance.[1] Therefore, there is a need for the development of new cancer therapies with greater therapeutic efficiency and fewer adverse effects. Photothermal therapy (PTT), which can convert absorbed light into localized heat to ablate cancer cells, has been recognized as a noninvasive and cancer-specific therapy by combining and using specific light excitation with a well-designed photothermal agent.[2,3] Among different external light sources, near-infrared (NIR) light (λ = 700−1100 nm) is particularly attractive for photothermal therapy because of its minimal absorbance by normal tissues, thereby allowing for noninvasive and relatively deep tissue penetration.[4,5] As a result, increased efforts have been devoted in the past decade to develop a new class of NIR-absorbing nanomaterials for PTT applications.

The currently available photothermal agents mainly comprise noble metal nanomaterials (Au,[2,6,7] Ag,[8] Pd,[9−11] and Ge[12]), carbon nanomaterials (carbon nanotube[13−16] and graphene[17,18]), semiconductor nanomaterials (Cu_xS,[19−21] Cu_xSe,[22] and Cu_xTe[23]), and two-dimensional transition metal dichalcogenides (MoS_2[24] and WS_2[25]). However, the majority of these currently used photothermal agents are nonbiodegradable and would retain in the body for a very long period, probably resulting in long-term toxicity of these materials.[26] Therefore, some conjugated polymers, such as polyaniline,[27] dopamine-melanin,[28] poly(3,4-ethylenedioxythiophene) poly(styrenesulfonate),[29] and polypyrrole (PPY) nanoparticles,[26,30−34] have been demonstrated to induce photothermal effects both *in vitro* and *in vivo*. Among them, PPY is known as a biocompatible conductive polymer, which has been widely used in many biomedical applications, such as biosensors, tissue engineering, and drug delivery.[35−37] Benefiting from its high conductivity and good biocompatibility, PPY has been demonstrated to support the adhesion and growth of different cell types and does not irritate the immune system of mammalians in some previous *in vitro* and *in vivo* studies.[37,38]

Received: December 15, 2014
Accepted: February 9, 2015
Published: February 9, 2015

DOI: 10.1021/am508837v
ACS Appl. Mater. Interfaces 2015, 7, 4354−4367

Recent *in vivo* studies have further demonstrated that PPY nanoparticles have very low long-term cytotoxicity and are attractive candidates for biomedical applications.[30,39] In addition, several recent studies have suggested that PPY can potentially serve as a new PTT agent for photothermal treatment of cancer owing to its strong NIR absorbance and high photothermal conversion efficiency.[26,30−34] However, the photothermal application of PPY based materials is still in its infancy; further research is required to develop new PPY-based nanoplatforms for cancer treatment.

In recent years, theranostics, which combines diagnostic and therapeutic modalities within a single platform so as to obtain optimized therapeutic efficacy, has evolved as a new paradigm in cancer therapies.[40] Therefore, an ideal theranostic agent should not only allow the treatment of cancer by photothermal effect and/or targeted delivery of therapeutic agents but also provide reliable assessment of the detailed tumor characteristics such as location, size, and shape via various imaging modalities.[3,41] To this end, much effort has been dedicated to explore new multifunctional photothermal platforms by incorporation of different imaging modalities into NIR-absorbing polymers for imaging-guided photothermal therapies.[5,34,42−45] Au and superparamagnetic iron oxide (Fe_3O_4) nanomaterials have provided many exciting opportunities for the development of theranostic agents due to their inherent advantages.[46−50] Since Au element provides almost three times greater X-ray attenuation per unit weight than iodine, gold nanomaterials hold great potential as contrast agents for X-ray computed tomography (CT) imaging applications. Concurrently, Au nanomaterials with diversified morphologies are also good photothermal agents because they have strong optical adsorption in the red and NIR regions,[40,51,52] while Fe_3O_4 is currently considered as a promising contrast enhancement agent for magnetic resonance imaging (MRI).[40,53] Therefore, a well-prepared nanocomposite by combining Au, Fe_3O_4, and PPY into one agent would provide an attractive theranostic platform for simultaneous imaging-guided diagnosis and photothermal therapy. In such nanocomposites, Au and iron oxide components may respectively enhance the capacity of nanocomposites as contrast agents for magnetic resonance (MR) and CT imaging, thus allowing a real-time imaging-guided photothermal therapy and the following post-therapeutic evaluation. In addition, the combination of both photothermal agents PPY and Au into a single nanocomposite would provide enhanced photothermal conversion efficiency. Although few studies on the integration PPY with single inorganic nanostructures for photothermal therapy and imaging-guided therapy have been reported most recently,[32,34,42,45,54] the simultaneous integration of PPY, Fe_3O_4, and Au nanorods (Au NRs) into a multifunctional theranostic platform for dual-modal imaging-guided photothermal therapy has not yet been demonstrated to our best knowledge.

Here, we report a very simple synthesis of monodisperse Au/PPY@Fe_3O_4 nanocomposites. A NIR-absorbing conjugated polymer, PPY, was first used to encapsulate Au NRs and obtain Au/PPY nanoparticles by iron cation-mediated oxidation polymerization. After this process, a large number of ferric (Fe^{3+}) and ferrous ions (Fe^{2+}) remained in the obtained Au/PPY nanoparticles. These residual Fe ions subsequently served as precursors to form Fe_3O_4 crystals *in situ* on the surface of presynthesized Au/PPY nanoparticles and thus obtain a theranostic agent for simultaneous MR/CT dual-imaging and photothermal therapy of cancer. Furthermore, the molar extinction coefficient, NIR photothermal conversion efficiency, and biocompatibility of the developed nanocomposites were demonstrated by *in vitro* studies.

2. EXPERIMENTAL SECTION

2.1. Materials. Cetyltrimethylammonium bromide (CTAB), poly(vinyl alcohol) (PVA, 88% hydrolyzed, average molecular weight 8800), Triton X-100, and bovine serum albumin (BSA) were purchased from Sigma-Aldrich (Shanghai) Trading Co., Ltd. (Shanghai, China). Pyrrole (99%) and iron(III) chloride hexahydrate ($FeCl_3{\cdot}6H_2O$, 99%) were both obtained from Aladdin (Shanghai, China). Ammonium hydroxide (NH_4OH, 28.0−30.0%), sodium borohydride ($NaBH_4$, 96%), L-ascorbic acid, silver nitrate ($AgNO_3$), and chloroauric acid tetrahydrate ($HAuCl_4{\cdot}4H_2O$) were obtained from Sinopharm Chemical Reagent Co., Ltd. (Shanghai, China). Fetal bovine serum (FBS), penicillin-streptomycin, trypsin, and Dulbecco's modified Eagle's medium (DMEM) were purchased from Gibco Life Technologies (Grand Island, USA). Paraformaldehyde was obtained from Beijing Dingguo Changsheng Biotechnology Co., Ltd. (Beijing, China). Alexa Fluor 488 conjugated phalloidin was obtained from Molecular Probes (Invitrogen, USA). Trypan blue and Cell Counting Kit-8 (CCK-8) were purchased from Beyotime Institute of Biotechnology (China). All other chemicals and solvents were obtained from Adamas-beta Inc. (shanghai, China). Deionized (DI) water with resistivity of 18.2 Ω was used throughout the experiments. All chemicals were used as received without further purification.

2.2. Preparation of Gold Nanorods (Au NRs). Au NRs were foremost synthesized through a seed-mediated method as previously described with some minor modifications.[55,56] In a typical synthesis, CTAB-modified gold seeds were first synthesized by chemical reduction of $HAuCl_4$ with $NaBH_4$. $HAuCl_4$ (3 mL, 411.9 mg/mL) was added to a freshly prepared CTAB solution (5 mL, 72.8 mg/mL). Then, ice-cold $NaBH_4$ (1.2 mL, 378.3 μg/mL) was added to the above stirred mixture solution. After vigorous stirring, seeds formed immediately and were kept at room temperature within 2−5 h. The growth solution for Au NRs was prepared by mixing CTAB (100 mL, 72.8 mg/mL), $AgNO_3$ (5.6 mL, 679.5 μg/mL), $HAuCl_4$ (10 mL, 5.1 mg/mL), and DI water (90 mL). Ascorbic acid (2.5 mL, 14.9 mg/mL) was slowly added to the aforementioned mixture. This was followed by addition of a 2 mL as-synthesized seeds solution to the growth medium. The resulting solution was kept at 30 °C, and the color of the solution gradually changed within 15 min. To remove excess CTAB surfactant, the as-obtained Au NRs were collected by centrifugation of 30 mL aliquots at 12000 rpm for 30 min. After discarding the supernatant, the precipitate was dispersed in 1 mL of DI water for the next step to synthesize the polypyrrole-coated Au NRs hybrid nanoparticles.

2.3. Preparation of Gold/Polypyrrole (Au/PPY) Nanoparticles. The coating of PPY on Au NRs was carried out by iron cation-mediated oxidation polymerization. As soon as Au NRs were synthesized, 1 mL of aqueous solution of Au NRs, 373 mg of $FeCl_3$, and 10 mL of PVA (8%) aqueous solution were mixed under vigorous stirring for 1 h and by sonication for another 0.5 h. Subsequently, 69.2 μL of pyrrole monomer was added dropwise into the above solution at 4 °C. After being stirred for 20 s, the reaction mixture was incubated at the same temperature for 4 h to ensure pyrrole monomer complete oxidative polymerization. The resulting dark Au/PPY nanoparticle solution was directly used for the next step to synthesize the Au/PPY@Fe_3O_4 nanocomposites.

2.4. Preparation of Gold/Polyrrole@Fe_3O_4 (Au/PPY@Fe_3O_4) Nanocomposites. Briefly, 2 mL of the Au/PPY nanoparticle solution obtained in the above step was diluted with 12 mL of DI water and 1.6 mL of ethanol, and the mixture was heated to 70 °C under N_2 atmosphere with vigorous stirring. Following this step, 0.8 mL of NH_4OH (1%) solution was quickly added to the reaction solution at 70 °C under N_2 atmosphere. After 0.5 h, an additional 0.8 mL of 1% NH_4OH was quickly injected, and the reaction was kept at 70 °C for another 0.5 h. Then, the mixture aqueous dispersion of the Au/PPY@Fe_3O_4 nanocomposites was cooled down and was kept under room

DOI: 10.1021/am508837v
ACS Appl. Mater. Interfaces 2015, 7, 4354−4367

temperature. The black precipitate was collected by sedimentation with the help of an external magnetic field with water for several times to remove excess reactants. The final products were dispersed in water under ambient conditions. The concentration of the Au/PPY@Fe_3O_4 nanocomposites was measured as the following method. Briefly, a 5 mL centrifuge tube was first weighed and marked as M_1 (mg). Then, 1 mL of as-synthesized Au/PPY@Fe_3O_4 nanocomposites solution was placed in the preweighed centrifuge tube and freezed-dried. The centrifuge tube with the freeze-dried nanocomposites was weighed and marked as M_2 (mg). Thus, the concentration of Au/PPY@Fe_3O_4 nanocomposites can be calculated in mg/mL as the difference between M_2 and M_1. Data are from the experiment replicated three times.

2.5. Characterization. The morphology and size of the synthesized nanocomposites were characterized by transmission electron microscopy (TEM). TEM studies were performed on a JEM-2100F (JEOL Ltd., Japan) transmission electron microscope operating at an acceleration voltage of 200 kV. The particle size distributions of Au/PPY@Fe_3O_4 nanocomposites were determined by dynamic light scattering (DLS) using a BI-200SM multiangle dynamic/static laser scattering instrument (Brookhaven, USA). The average PPY shell thickness of nanocomposites was obtained from at least 20 measurements on typical TEM images using ImageJ 1.4 G software (NIH, USA). Fourier transform infrared spectroscopy (FTIR) spectra were performed by a Nexus 670 (Thermo Nicolet, USA) spectrometer using KBr pellets. A powder X-ray diffraction (XRD) pattern was measured on a D/MAX-2550PC (Rigaku Inc., Japan) diffractometer with the Cu−Kα radiation at 45 kV and 40 mA. The X-ray photoelectron spectroscopy (XPS) were performed by using a PHI 5300 ESCA XPS (Philadelphia, USA) spectrometer with monochromatic Mg−K_α radiation as the excitation source. The Raman spectra were recorded at room temperature by using an inVia-Reflex micro-Raman spectroscopy system (Renishaw, UK) with a 633 nm solid laser of 50 mW power. UV−vis-NIR absorption spectra were obtained using a Lambda 35 UV−vis spectrophotometer (PerkinElmer, USA) at room temperature under ambient conditions. The Fe and Au concentration of the nanocomposite solution was analyzed using a Leeman Prodigy Inductively Coupled Plasma-Atomic Emission Spectroscopy (ICP-AES) system (Hudson, NH03051, U.S.A). Magnetic property measurement was carried out at room temperature using a vibrating sample magnetometer (VSM, Model 4 HF) with a maximum field of 7×10^6 A/m. MRI *in vitro* was performed with a 0.5 T MicroMR-20 system (Shanghai Niumag Corporation, China). The samples were diluted in water with iron (Fe) concentration in the range of 0−0.5 mM. The instrumental parameters of a T_2-weighted MRI were as follows: point resolution of 156 mm × 156 mm, section thickness of 0.8 mm, repetition time (TR) of 2000 ms, echo time (TE) of 30 ms, and number of excitation of 1. The T_2 relaxivity was calculated by a linear fit of the inverse T_2 ($1/T_2$) relaxation time as a function of Fe concentration (mM). The *in vitro* CT signal measurement of Au/PPY@Fe_3O_4 was evaluated by using on a multidetector CT scanner (Briliance 64, Philips Healthcare, The Netherlands), with the following acquisition parameters: tube voltage 120 kV, X-ray energy 80 keV, tube current 179 mA, pitch 0.3, field-of view (FOV) 233 mm, and slice thickness 0.8 mm. The X-ray attenuation values of the samples were calculated on the same workstation using the software supplied by the manufacturer in Hounsfield Units. Each experiment was obtained in triplicate.

2.6. Photothermal Performance of Au/PPY@Fe_3O_4 Nanocomposites in Aqueous Solutions. To measure the photothermal heating performances of the as-synthesized Au/PPY@Fe_3O_4 nanocomposites, an 808 nm NIR laser was employed to deliver perpendicular through a quartz cuvette containing aqueous dispersion (0.5 mL) of Au/PPY@Fe_3O_4 nanocomposites with different concentrations (0, 0.05, 0.09, 0.18, 0.35, 0.70, 1.40, and 2.80 mg/mL). Water was used as a control. The NIR laser light source was equipped with an external adjustable power (0−5 W/cm^2) 808 nm semiconductor laser device with a 5 mm diameter laser module (Tours Radium Hirsh Laser Technology Co., Ltd., Xi'an, China). The output power was independently calibrated by using a hand-held model 1918-C optical power meter (Newport Corp. CA, USA). The temperature was measured one time per 10 s using a thermocouple thermometer (DT-8891E, Shenzhen Everbest Machinery Industry Co., Ltd., China) which was inserted into the aqueous dispersion perpendicular to the path of the laser light with an accuracy of ±1 °C.

To measure the photothermal conversion efficiency (η), the temperature change of the Au/PPY@Fe_3O_4 dispersion was recorded as a function of time under continuous irradiation of the 808 nm laser with a power density of 2 W/cm^2 until the solution reached a steady-state temperature. The η value was calculated by eq 1[57]

$$\eta = \frac{hS(T_{max} - T_{Surr}) - Q_S}{I(1 - 10^{-A_{808}})} \quad (1)$$

where h is the heat transfer coefficient, S is the surface area of the container, T_{max} is the equilibrium temperature, T_{Surr} is the ambient temperature of the surroundings, Q_S expresses the heat associated with the light absorbance, I is the incident laser power, and A_{808} is the absorbance of the Au/PPY@Fe_3O_4 nanocomposites at 808 nm.

2.7. *In Vitro* Hemolysis Assay. Fresh blood samples were collected from mice and stabilized with heparin. For hemolysis assay, red blood cells (RBCs) were obtained according to our previous studies.[58,59] Briefly, RBCs were separated from serum by centrifugation at 3000 rpm for 10 min at 4 °C and further purified more than five times with phosphate buffered saline (PBS) buffer. The RBCs were then diluted 10 times with PBS. After that, 300 μL of diluted RBCs suspension was taken out to mix with (i) Au/PPY@Fe_3O_4 suspensions in 1.2 mL of PBS at concentrations from 0.05 to 2.80 mg/mL, (ii) 1.2 mL of PBS as negative control, and (iii) 1.2 mL of DI water as positive control, respectively. Then, all the mixtures were gently shaken and kept for 3 h at 37 °C, followed by centrifugation at 3000 rpm for 3 min. The absorbance values of the supernatants at 541 nm were measured by using UV−vis spectrophotometer. The hemolysis percent of RBCs in each sample was calculated as eq 2, and the average value was obtained from five parallel samples

$$\text{Hemolysis\%} = \frac{A_{Sample} - A_{Negative\ control}}{A_{Positive\ control} - A_{Negative\ control}} \times 100\% \quad (2)$$

where A_{Sample}, $A_{Negative\ control}$, and $A_{Positive\ control}$ are the absorbance of samples and the negative control and positive control, respectively.

2.8. Cell Lines and Cell Culture. A human cervix adenocarcinoma cell line (HeLa cell), a mouse leukemic monocyte macrophage cell line (RAW 264.7), and a mouse fibroblast L929 cell line were obtained from Shanghai Institute of Cell Biology, Chinese Academy of Sciences (Shanghai, China). Cells were grown in normal DMEM culture medium supplemented with 10% FBS, 1% 100 U/mL penicillin, and 100 μg/mL streptomycin. The cells were maintained in a humidified atmosphere of 95% air and 5% CO_2 at 37 °C. The culture medium was changed every 2 days, and cells were passaged by trypsinization before confluence.

2.9. *In Vitro* Cytotoxicity Assay of Au/PPY@Fe_3O_4 Nanocomposites. The *in vitro* cytotoxicity of the Au/PPY@Fe_3O_4 nanocomposites was performed by CCK-8 assay. Briefly, HeLa, RAW 264.7, and L929 cells were respectively seeded into 96-well plates at the densities of 10^4 cells per well and cultured for 24 h to allow cells to attach. Afterward, the original culture medium was changed with fresh medium (blank control), and Au/PPY@Fe_3O_4 dispersions were diluted with medium at the desired concentrations (0.02, 0.05, 0.09, 0.18, 0.35, 0.7, 1.4, and 2.8 mg/mL, respectively) for 24 and 48 h. Then the medium was removed and replaced by 10 μL CCK-8 solutions in 100 μL of serum-free medium. After incubation for another 2 h at 37 °C, the absorbance of each well at 450 nm was read by a microplate reader (MK3, Thermo, USA). The relative cell viability was calculated by eq 3, and five replicates were carried out for each treatment group

$$\text{Cell viability (\%)} = \frac{A_{Test}}{A_{Control}} \times 100\% \quad (3)$$

where A_{Test} and $A_{Control}$ are the absorbance of cell treated with and without Au/PPY@Fe_3O_4 nanocomposites, respectively.

DOI: 10.1021/am508837v
ACS Appl. Mater. Interfaces 2015, 7, 4354−4367

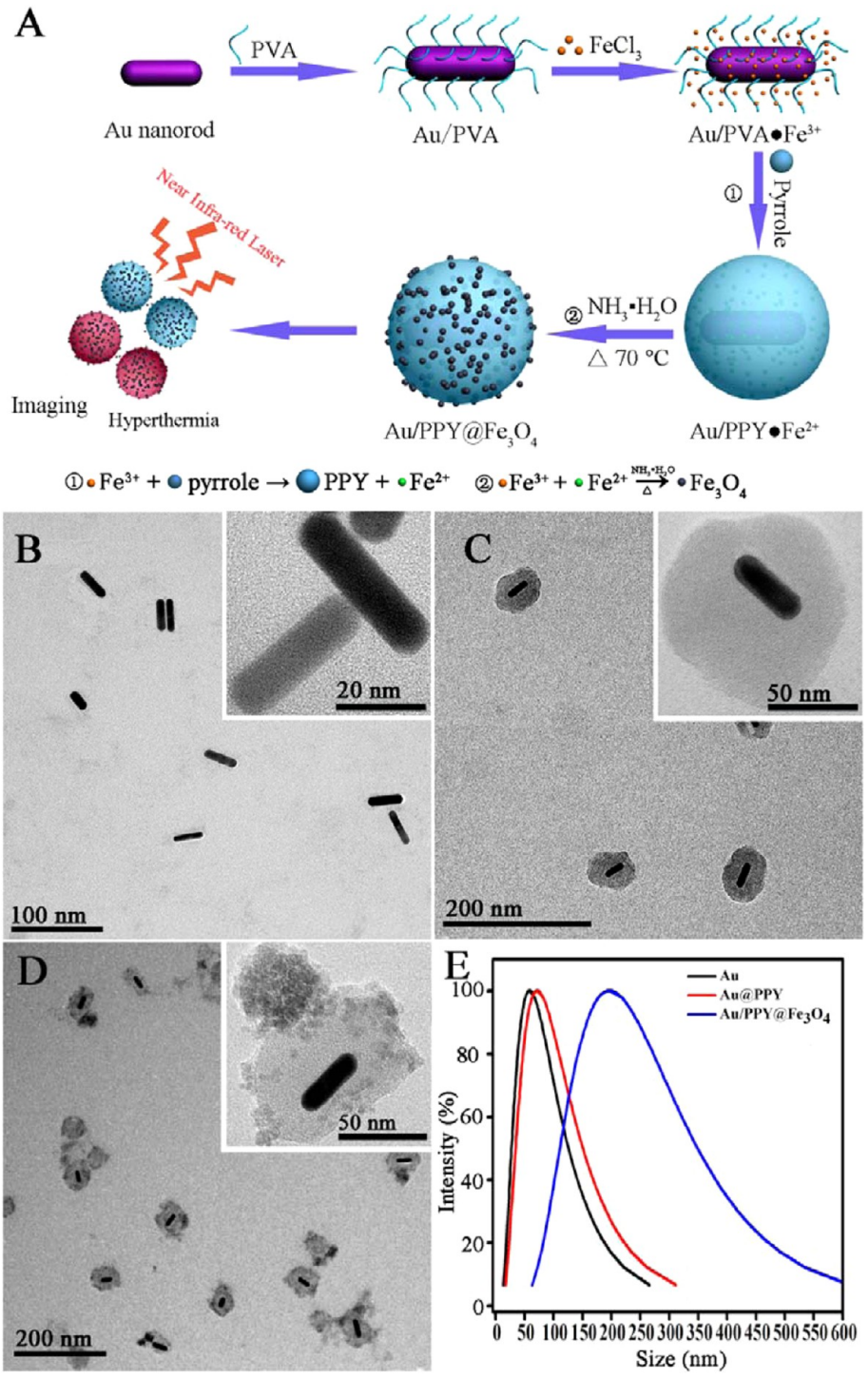

Figure 1. (A) Schematic illustration of the synthetic route to the Au/PPY@Fe_3O_4 nanocomposites. TEM images of (B) Au NRs, (C) Au/PPY composite nanoparticles, and (D) Au/PPY@Fe_3O_4 nanocomposites. The insets show the TEM images of the corresponding individual particle. (E) The particle size distribution of Au NRs, Au/PPY nanoparticles, and Au/PPY@Fe_3O_4 nanocomposites measured by the DLS test.

2.10. *In Vitro* Photothermal Ablation of Au/PPY@Fe_3O_4 Nanocomposites for Cancer Cells. HeLa cells were first plated in a 24-well plate at a density of 2×10^4 cells per well for 24 h prior treatment. Thereafter, the culture medium was changed, and cells were divided into four groups: group 1 with cells only; group 2 incubated with Au/PPY@Fe_3O_4 nanocomposites only; group 3 incubated with NIR only; and group 4 incubated with Au/PPY@Fe_3O_4 nanocomposites + NIR. After incubation for 2 h, the cells of group 3 and 4 were exposed to an 808 nm laser at a power density of 2.0 W/cm^2 for 5 min. For trypan blue staining, all the cells were stained by 0.4% trypan blue solution for 5 min. Then trypan blue was washed by PBS, and the images of the labeled cells were examined immediately using a light microscope (Olympus, BH-2). Each experiment was performed three times.

2.11. Assessing the Effect of Nanocomposites-Mediated Photothermal Ablation on Cell Cytoskeleton. To assess the effect of nanocomposites on cell cytoskeleton, HeLa cells (10^5 cells per dish) were seeded into 20 mm glass bottom culture dishes and incubated for 24 h. After that, the medium was removed, and the cells were divided into four groups as above-mentioned. Then the cells of group 3 and 4

DOI: 10.1021/am508837v
ACS Appl. Mater. Interfaces 2015, 7, 4354−4367

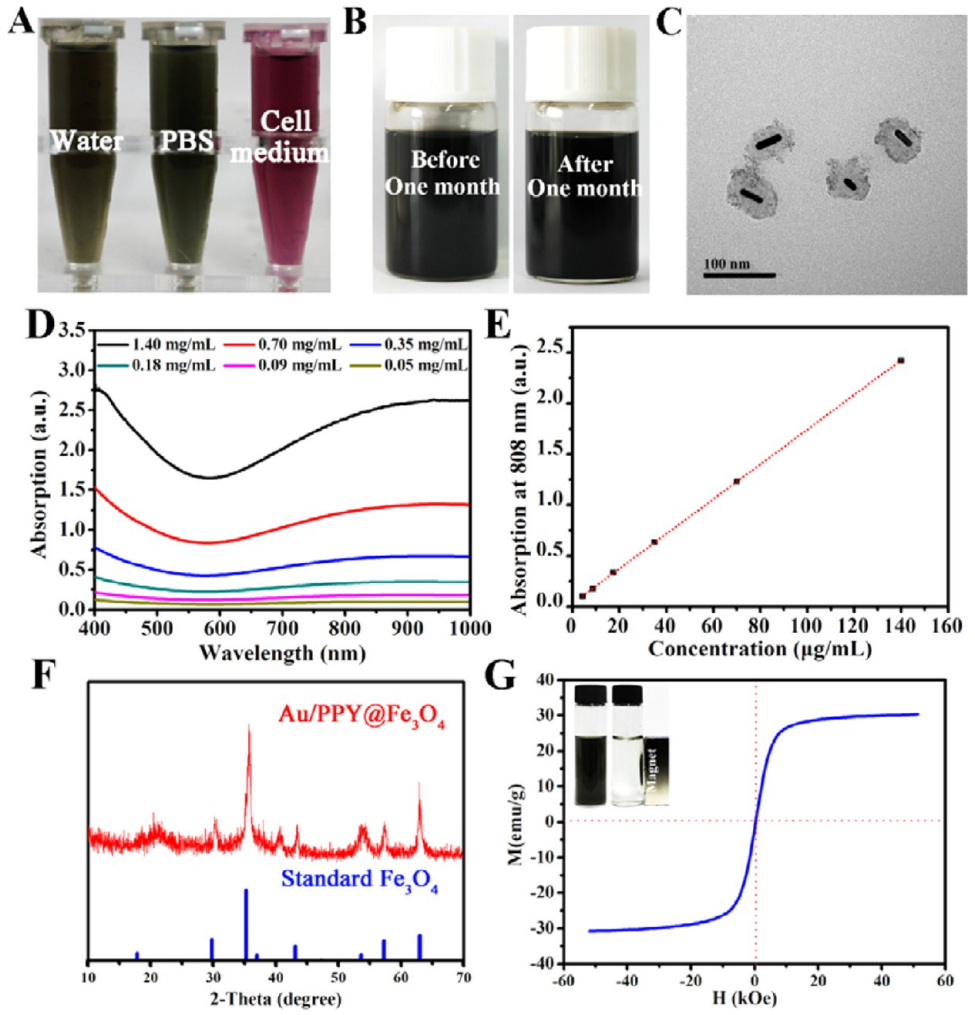

Figure 2. (A) Digital photographs of Au/PPY@Fe_3O_4 nanocomposites dispersions with a concentration of 0.5 mg/mL in (left) distilled water, (middle) PBS buffer, and (right) cell culture medium for at least 7 days. (B) Digital photographs of the Au/PPY@Fe_3O_4 nanocomposite dispersion with a concentration of 2.8 mg/mL in PBS buffer (left) before and (right) after being settled for one month. (C) TEM image of the Au/PPY@Fe_3O_4 nanocomposite stored in PBS buffer for one month. (D) UV−vis-NIR absorption spectra of the Au/PPY@Fe_3O_4 nanocomposite dispersed in distilled water at various concentrations. (E) Linear fitting of the absorption strength of Au/PPY@Fe_3O_4 dispersion at 808 nm versus the particle concentrations. (F) X-ray diffraction pattern of the Au/PPY@Fe_3O_4 nanocomposites, as reference by the standard face-centered cubic Fe_3O_4 phase (JCPDS file number 65-3107). (G) Magnetization curve of the Au/PPY@Fe_3O_4 nanocomposites. The insets show that the Au/PPY@Fe_3O_4 nanocomposites can be collected from the dispersion by using a magnet.

were exposed to an 808 nm laser at a power density of 2.0 W/cm^2 for 10 min. All the cells were then incubated again at 37 °C for 12 h. After this treatment, the culture medium was removed, and the HeLa cells were rinsed twice with prewarmed PBS buffer and fixed with paraformaldehyde (4%) for 20 min. The fixed cells were washed two or more times with PBS and then permeabilized with 0.1% Triton X-100 in PBS for 5 min, followed by blocking with 1% BSA in PBS for 30 min. After washing with PBS, the cells were subjected to F-actin staining with Alexa Fluor 488 conjugated phalloidin for 30 min at room temperature. After extensively washing with PBS to remove unbound dyes, the stained cells were observed by a Carl Zeiss LSM 700 confocal lasers scanning microscope (CLSM, He−Ne and Ar lasers). The untreated cells were used as the control in all the above fluorescence staining experiments. The *in vitro* photothermal ablation (PTA) efficiency of the Au/PPY@Fe_3O_4 nanocomposites against HeLa cells was performed by CCK-8 assay.

2.12. Assessing the Integrity of the Lysosomal Membrane. The integrity of the lysosomal membrane was examined by using acridine orange (AO) staining. For AO staining, HeLa cells (10^5 cells per dish) were seeded into 20 mm glass bottom culture dishes and incubated for 24 h. After that, the medium was removed, and the cells were divided into four groups in the same manner as above-mentioned. HeLa cells were rinsed twice with PBS and were stained by using AO (5 μg/mL) in complete medium at 37 °C for 15 min. After further washing with PBS, serum-free medium was added into the wells, and cells were observed by CLSM. AO was excited at 488 nm, and emission signals were detected at 530 nm (green color) and 590 nm (red color).

2.13. Statistical Analysis. All quantitative values were expressed as the mean ± standard deviation (SD). The statistical significance of differences between experimental and control groups was carried out by using one-way analysis of variance (one-way ANOVA) and Scheffe's post hoc test. The statistical significance for all tests was at $*P < 0.05$ and $**P < 0.01$.

3. RESULTS AND DISCUSSION

3.1. Synthesis Au/PPY@Fe_3O_4 Nanocomposites. The strategy designed in this study is iron cation-mediated PPY oxidation polymerization on the surface of Au NRs and subsequent forming magnetic iron oxide nanocrystals on the outer shell of the Au/PPY nanocomposites in the presence of Fe^{2+} and Fe^{3+} under alkaline conditions. Figure 1A schemati-

DOI: 10.1021/am508837v
ACS Appl. Mater. Interfaces 2015, 7, 4354−4367

cally illustrated the overall synthetic protocol for Au/PPY@Fe_3O_4 nanocomposites. Specifically, water-soluble PVA serves as a dispersion aid for improving the stability of Au NRs solution and $FeCl_3$ was used to supply Fe^{3+} ions. The PVA/Fe^{3+} complex could be spontaneously formed in an aqueous phase. In the next step, the pyrrole monomer was introduced into the complex aqueous solution, thus the PPY shell was coated onto the outer surface of the Au NRs through oxidative polymerization of pyrrole induced by Fe^{3+} ions. Meanwhile, the formed Au/PPY nanocomposites were modified by PVA, which functioned as a capping agent to make the particles highly hydrophilic as well as to control the particles size.[30,33,60] For the subsequent experiment of forming Fe_3O_4 *in situ* on the Au/PPY nanocomposites, an ammonia solution was dropped into the system with moderate heating at 70 °C to coprecipitate the reduced Fe^{2+} ions and unreacted Fe^{3+} ions without any additional iron precursors.[61,62]

3.2. Characterization of Au/PPY@Fe_3O_4 Nanocomposites. In order to confirm our hypothesis, TEM studies were carried out by drop-casting sample solutions onto a carbon-coated copper grid. First of all, a representative TEM image of Au NRs with an average aspect ratio (length to diameter ratio) of ∼3 is shown in Figure 1B. After being coated with a compact PPY layer by oxidation polymerization of pyrrole, the obtained Au/PPY nanocomposites with a PPY layer of ∼32 nm in thickness exhibited a clear core−shell structure because of the different electron contrast between Au NR and PPY as illustrated in Figure 1C. Subsequently, as shown in Figure 1D, the resultant Au/PPY nanocomposites were further hydrothermally reacted with an ammonia solution to generate Fe_3O_4 nanocrystals with sizes ranging from 5 to 10 nm capped on the outer surface of Au/PPY nanocomposites. Furthermore, the obtained sandwich-shape core−shell structure with a mean diameter of around 200 nm is composed of an Au NR core about 60 nm in diameter, a Fe_3O_4 outer shell of around 70 nm in thickness, and a PPY inner layer between the core and the shell, as indicated by the DLS data revealed in Figure 1E. The ICP-AES was employed to measure that Fe_3O_4 and Au accounted for 22.5 ± 5.4% and 15.8 ± 3.1%, respectively.

The stability of nanocomposites in a biologic system is very important for their biomedical applications. As shown in Figure 2A, the Au/PPY@Fe_3O_4 nanocomposites could be readily dispersed in DI water, PBS buffer, and serum-containing cell culture medium to form a homogeneous suspension, and no sediment appeared for at least 7 days. Au/PPY@Fe_3O_4 dispersions exhibit a well-dispersed state in PBS even at the concentration up to 2.8 mg/mL for one month (Figure 2B). Note that after being dispersed in PBS for a long time, the nanocomposites did not show any sensible changes including particle size distribution (Figure S2) and morphology, and no separation of Fe_3O_4 from the Au/PPY@Fe_3O_4 nanocomposites, which is beneficial to MRI and CT application. The optical property of the aqueous dispersion containing Au/PPY@Fe_3O_4 nanocomposites with various concentrations were examined by UV−vis-NIR spectroscopy, as shown in Figure 2D. The aqueous dispersion of the Au/PPY@Fe_3O_4 nanocomposites exhibited a minimum absorption of around 580 nm and showed an intense and broad absorption band extending from the visible to the NIR region with maximum at nearly 950 nm (Figure 2D), which is assigned to bipolaron band transitions for PPY.[63] Such a strong absorption of as-prepared nanocomposites in the NIR region means the potential for photothermal conversion performance upon 808 nm laser irradiation. Moreover, the absorptions at 808 nm were linearly enhanced with an increase of the particle concentration even after having been settled for 7 days, which also means no precipitate formed in this period and further demonstrated the good dispersibility of the Au/PPY@Fe_3O_4 nanocomposites in PBS (Figure 2E).[33] The presence of characteristic chemical groups on the samples is identified by using FTIR spectroscopy. For the spectrum of the Au/PPY@Fe_3O_4 nanocomposites (Figure S3), a broad peak at about 3432 cm^{-1} corresponds to N−H stretching in the pyrrole ring or −OH stretching vibrations in the PVA.[64,65] Two peaks at 2855 and 2932 cm^{-1} are associated with the symmetric and asymmetric vibrations of CH_2.[66] The band at 1633 cm^{-1} is attributed to the C═N stretching vibrations, and the 1400 cm^{-1} peak is associated with the stretching of C−N in polypyrrole[67] or C−C stretching vibrations. The band at 1554 cm^{-1} corresponds to the ring stretching vibrations of the C═C bond.[68] The band at 1300 cm^{-1} corresponds to the ═C−H band in plane vibration.[69,70] The band appeared at 1076 cm^{-1}, which may be assigned to the C−N[64] or Fe−O−C stretching vibrations.[65] The adsorption band in 460 cm^{-1} corresponds to the stretching vibrational frequency of the Fe−O bond introduced by Fe_3O_4 nanoparticles.[64] Figure 2F shows the X-ray diffraction pattern of the core−shell nanocomposites. Since the XRD patterns of Fe_3O_4 and Fe_2O_3 are very similar,[71] Raman spectroscopy and XPS were further performed to confirm the growth of Fe_3O_4 in the nanocomposites. Figure S4A indicates the Raman spectroscopy measured for the as-synthesized Au/PPY@Fe_3O_4 nanocomposites. It showed the characteristic peak at 670 cm^{-1}, which is unambiguously attributed to the A_{1g} vibrational mode, confirming that the as-synthesized nanocomposites are composed of the Fe_3O_4 phase.[71] Figure S4B showed the XPS spectrum of the Au/PPY@Fe_3O_4 nanocomposites. The appearance of the characteristic peaks of 713.6 and 726.4 eV, corresponding to Fe $2p_{3/2}$ and Fe $2p_{1/2}$, respectively, further supports that Fe^{3+} and Fe^{2+} states coexisted in the nanocomposites;[72−74] and as mentioned above, the adsorption band of 460 cm^{-1} in FTIR corresponds to the stretching vibrational frequency of the Fe−O bond introduced by Fe_3O_4 nanoparticles. These combined results indicated that Fe_3O_4 has been synthesized in the nanocomposites. From the above characterization, it could be deduced that Fe_3O_4 nanoparticles were on the surface of the nanocomposites. In order to further reveal the position of the Fe_3O_4 nanoparticles, the as-synthesized Au/PPY@Fe_3O_4 nanocomposites solution was further treated with 2 mL of hydrochloric acid (HCl, 1 M) and then for TEM imaging (Figure S5). Before the Au/PPY@Fe_3O_4 nanocomposites were treated with HCl, a typical sandwich structure with an Au NRs core, a PPY layer in the middle layer, and many Fe_3O_4 nanoparticles in the outer layer could be clearly observed (Figure 1D, Figure S5A and B). Interestingly, after having been treated with HCl, the nanocomposites exhibited a clear "core-shell" structure with an Au NRs core and a nonporous PPY outer shell (Figure S5C), indicating most of the Fe_3O_4 nanoparticles were on the surface of the nanocomposites; and only a small percentage of Fe_3O_4 are randomly embedded in the surface of a polymer matrix, because some holes could be found on the outer layer of PPY in some nanocomposites (Figure S5D).

The magnetization hysteresis (M-H) loop curve of the Au/PPY@Fe_3O_4 nanocomposites was measured by sweeping the external magnetic field between −50 to 50 kOe at 25 °C. As shown in Figure 2G, the M-H loop showed no magnetization

DOI: 10.1021/am508837v
ACS Appl. Mater. Interfaces 2015, 7, 4354−4367

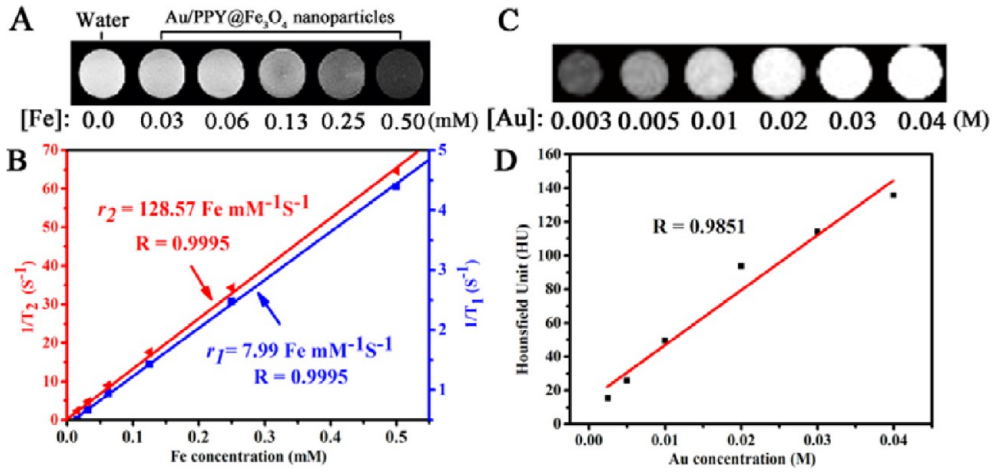

Figure 3. (A) T_2-weighted MRI photographs of the hydrophilic Au/PPY@Fe_3O_4 nanocomposites dispersed in PBS solution with different Fe concentrations. (B) The T_1 and T_2 relaxation rate of the Au/PPY@Fe_3O_4 nanocomposites as a function of the Fe concentration. (C) CT images of Au/PPY@Fe_3O_4 nanocomposites at different concentrations dispersed in PBS solution with different Fe concentrations. (D) X-ray attenuation intensity (HU) as a function of concentration of the Au concentration.

or coercivity, indicating that the superparamagnetic behavior makes the nanocomposite easily controlled by external magnetic field manipulation (the inset in Figure 2G). The M-H loop also revealed the saturation magnetization (M_s) of Au/PPY@Fe_3O_4 nanocomposites is 30.8 emu/g, which could facilitate MRI and targeted delivery application. However, the M_s value of nanocomposites is relatively low compared with the value for Fe_3O_4 reported in the literature (more than 75 emu/g).[75,76] The decrease in M_s may be due to that the nonmagnetic Au NRs and PPY were introduced into the nanocomposites.

3.3. MR Relaxometry and X-ray Attenuation Measurement. The potential of the prepared Au/PPY@Fe_3O_4 nanocomposites as the contrast agents was further examined. As shown in Figure 3A, the images revealed a clear iron concentration-dependent darkening effect (Fe concentration measured by ICP-AES). With the increase of iron concentrations, we noticed that the measured signal intensity of the T_2-weighted images was obviously decreased. Figure 3B illustrates the corresponding transverse relaxation ($1/T_2$, red line) and longitudinal relaxation rates ($1/T_1$, blue line) of protons in Au/PPY@Fe_3O_4 aqueous solution as a function of iron concentration, which were measured in a 0.5 T magnetic field with a spin−echo pulse sequence, and accordingly, both of the values of $1/T_1$ and $1/T_2$ were linearly increased. The transverse relaxivity (r_2, the transverse relaxation rate per mM of iron) and longitudinal relaxivity (r_1, the longitudinal relaxation rate per mM of iron) value of the Au/PPY@Fe_3O_4 are 128.57 mM^{-1} S^{-1} and 7.99 mM^{-1} S^{-1}, respectively, which were calculated from the slope of this plot in Figure 3B. Importantly, the r_2/r_1 ratio of the Au/PPY@Fe_3O_4 nanocomposites is 16.1. It should be noted that the relatively high r_2 or high r_2/r_1 value demonstrates that Au/PPY@Fe_3O_4 has the potential to be used as a good T_2-weighted negative contrast agent for sensitive MRI applications.

Since Au nanomaterials display a better X-ray attenuation property,[77] Au/PPY@Fe_3O_4 nanoparticles enriched with the Au element was anticipated to be a good contrast agent to enhance X-ray CT. The feasibility of Au/PPY@Fe_3O_4 as a CT contrast agent was next explored via acquiring the X-ray CT image of Au/PPY@Fe_3O_4 nanocomposites at different Au concentrations *in vitro* (Au concentration measured by ICP-AES). It can be seen that the brightness of the CT image for Au/PPY@Fe_3O_4 nanocomposites in aqueous solution increases with the molar concentration enhancement of Au (Figure 3C). The CT values of Au/PPY@Fe_3O_4 increased linearly as the Au concentration increases, as shown in Figure 3D, indicating that the Au/PPY@Fe_3O_4 could be utilized as a positive X-ray CT imaging contrast agent.

3.4. Measurement of Photothermal Performance. Another important attribute of the Au/PPY@Fe_3O_4 nanocomposites is their tunable photothermal effect. We first investigate the photothermal properties of aqueous solutions loaded with Au/PPY@Fe_3O_4 nanocomposites at various concentrations (0.05, 0.09, 0.18, 0.35, 0.7, 1.4, and 2.8 mg/mL) exposed to an 808 nm NIR laser at a power density of 2 W/cm^2. Remarkably, obvious concentration-dependent temperature increases of Au/PPY@Fe_3O_4 nanocomposites were found after continuous irradiation for 600 s, and the temperature of the solution can be precisely controlled from 25.4 to 62.7 °C by adjusting the composite content (Figure 4A and B). In marked contrast, insignificant heating with a temperature rise of only ~0.5 °C was observed for pure water under the same treatment conditions. To further investigate the photothermal conversion efficiency of those nanocomposites, as shown in Figure 4C and D, an Au/PPY@Fe_3O_4 solution with a low concentration of 1.4 mg/mL was exposed to an 808 nm continuous-wave laser at various laser power densities. The photothermal heating curves measured also showed a strong laser-power-dependent photothermal effect for Au/PPY@Fe_3O_4 nanocomposites with the highest temperature increment up to 60.4 °C. These results indicate that Au/PPY@Fe_3O_4 nanocomposites can rapidly and efficiently convert the energy from 808 nm laser into thermal energy. To further investigate the photothermal transduction ability of the Au/PPY@Fe_3O_4 aqueous solution, we recorded the temperature change of the sample solution with the concentration of 1.4 mg/mL as a function of time under the 808 nm laser at the power density of 2.0 W/cm^2 continuous irradiation for 600 s (Figure 4E and F). According to the obtained data and the reported method, the photothermal conversion efficiency of Au/PPY@Fe_3O_4 nanocomposites can reach 23.9% (Supporting Information). We thus believe these

DOI: 10.1021/am508837v
ACS Appl. Mater. Interfaces 2015, 7, 4354−4367

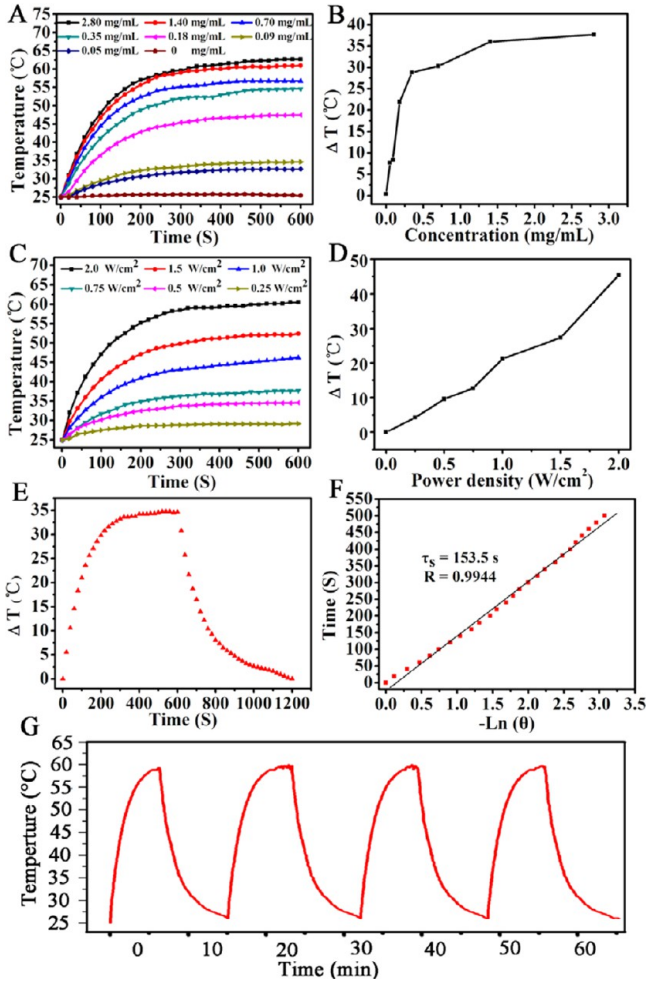

Figure 4. Photothermal profiles of Au/PPY@Fe_3O_4 nanocomposites. (A) Temperature profiles of pure water and Au/PPY@Fe_3O_4 dispersions with different concentrations (2.8, 1.4, 0.7, 0.35, 0.18, 0.09, and 0.05 mg/mL) as a function of 808 nm laser irradiation time for 10 min at a power density of 2 W/cm^2. (B) Plot of temperature change (ΔT) over a period of 10 min versus the particle concentration. (C) Photothermal heating curves of pure water and an Au/PPY@Fe_3O_4 solution at the concentration of 1.4 mg/mL under 808 nm laser irradiation at various power densities (0.25, 0.5, 0.75, 1, 1.5, and 2 W/cm^2) for 10 min. (D) Plot of temperature change (ΔT) over a period of 10 min versus the irradiation power density. (E) Photothermal effect of an aqueous dispersion of Au/PPY@Fe_3O_4 nanocomposites irradiated by using an 808 nm laser at a power density of 2 W/cm^2. The laser was turned off after irradiation for 10 min. (F) Plot of cooling time (after 600 s) versus negative natural logarithm of the driving force temperature obtained from a cooling stage as shown in (E). The time constant (τ_s) for heat transfer of the system is determined to be 153.5 s. (G) Temperature monitoring of an Au/PPY@Fe_3O_4 aqueous suspension at the concentration of 1.4 mg/mL during for successive cycles of an on-and-off laser.

nanocomposites have superior ability of NIR photothermal transduction and could be used for photothermal therapy.

To estimate the contribution of both PPY and Au NRs to the photothermal transduction of Au/PPY@Fe_3O_4 nanocomposites, the UV−vis-NIR spectra of Au NRs, PPY nanoparticles, and Au/PPY@Fe_3O_4 in DI water were recorded in the wavelength range 400−1000 nm (Figure S6A). The as-prepared Au NRs showed a typical longitudinal surface plasmon resonance (SPR) peak at around 750 nm. In contrast, both PPY and Au/PPY@Fe_3O_4 exhibited very similar strong light absorption characteristics from 650 to 1000 nm in the NIR region with a maximum light absorption peak at around 950 nm. The results suggest that PPY may play a predominant role in the photothermal conversion of Au/PPY@Fe_3O_4 nanocomposites. A recent study demonstrated that PPY nanoparticles showed higher photothermal conversion efficiency and NIR photostability than Au NRs at the same mass concentration.[30] In addition, the photothermal effect of different photothermal agents is dose-dependent.[30,54] In this study, the amount of PPY in the Au/PPY@Fe_3O_4 nanocomposites is about 61.7%, far more than 15.8% of the amount of Au NRs in the nanocomposites. Therefore, the photothermal conversion of the Au/PPY@Fe_3O_4 nanocomposites results mainly from PPY and slightly from Au NRs. As shown in Figure 4G, no significant decrease for the temperature elevation was observed for Au/PPY@Fe_3O_4 nanocomposites after four repeated laser on-and-off cycles (the laser was on for about 10 min in each cycle). The TEM image (Figure S6B) also indicates that the "rod-like" structure of Au NRs retained well in the nanocomposites after four cycles of laser irradiation. Thus, the synthesized Au/PPY@Fe_3O_4 nanocomposites possess good photostability and constant photothermal conversion behavior.

3.5. Hemocompatibility of Au/PPY@Fe_3O_4 Nanocomposites. Biocompatibility is an essential concern when it comes to the development of nanomaterials for biomedical application. Characterization of *in vitro* hemocompatibility of the nanocomposites has been considered to be one of the most important issues because biomedical applications require those nanocomposites contacting with blood. The influence of Au/PPY@Fe_3O_4 nanocomposites on hemolytic behavior of red blood cells (RBCs) was carried out to evaluate their biocompatibility, where DI water and PBS were denoted as positive and negative controls, respectively. As shown in Figure 5 A and B, when Au/PPY@Fe_3O_4 nanocomposites with different concentrations (0.05, 0.09, 0.18, 0.35, 0.7, 1.4, and 2.8 mg/mL) were exposed to the RBCs suspension, negligible hemolysis phenomenon is detected, similar to the negative PBS control. The hemolysis percentages of nanocomposites at different concentrations were quantified based on the absorbance of the supernatant at 541 nm (Figure 5A). It is found that the hemolysis percentages of particles are all less than 4% in the tested concentration range (0.05−2.8 mg/mL), indicating that Au/PPY@Fe_3O_4 nanocomposites possess admirable blood compatibility.

3.6. *In Vitro* Cytotoxicity of Au/PPY@Fe_3O_4 Nanocomposites. The ideal photothermal agent should be nontoxic or low-toxic for biological application. To evaluate the cytotoxicity of Au/PPY@Fe_3O_4 nanocomposites, the CCK-8 assay method was used. In order to get a reliable result, three kinds of cells including HeLa, L929, and RAW 264.7 cells were carried out in the cytotoxicity measurement experiment. According to the viabilities of the cells in Figure 5C-E, no obvious differences were found with and without the presence of Au/PPY@Fe_3O_4 nanocomposites, indicating that the synthesized Au/PPY@Fe_3O_4 nanocomposites appear to be largely biocompatible. The percentages of viable cells for HeLa cells, L929 cells, and RAW 264.7 cells were 81.9 ± 5.4%, 85.6 ± 7.6%, and 79.6 ± 10.7%, respectively, even exposure to nanocomposites with the concentration as high as 2.8 mg/mL for 48 h. The result strongly demonstrates that the Au/PPY@Fe_3O_4 nanocomposites have very low cytotoxicity. The good

DOI: 10.1021/am508837v
ACS Appl. Mater. Interfaces 2015, 7, 4354−4367

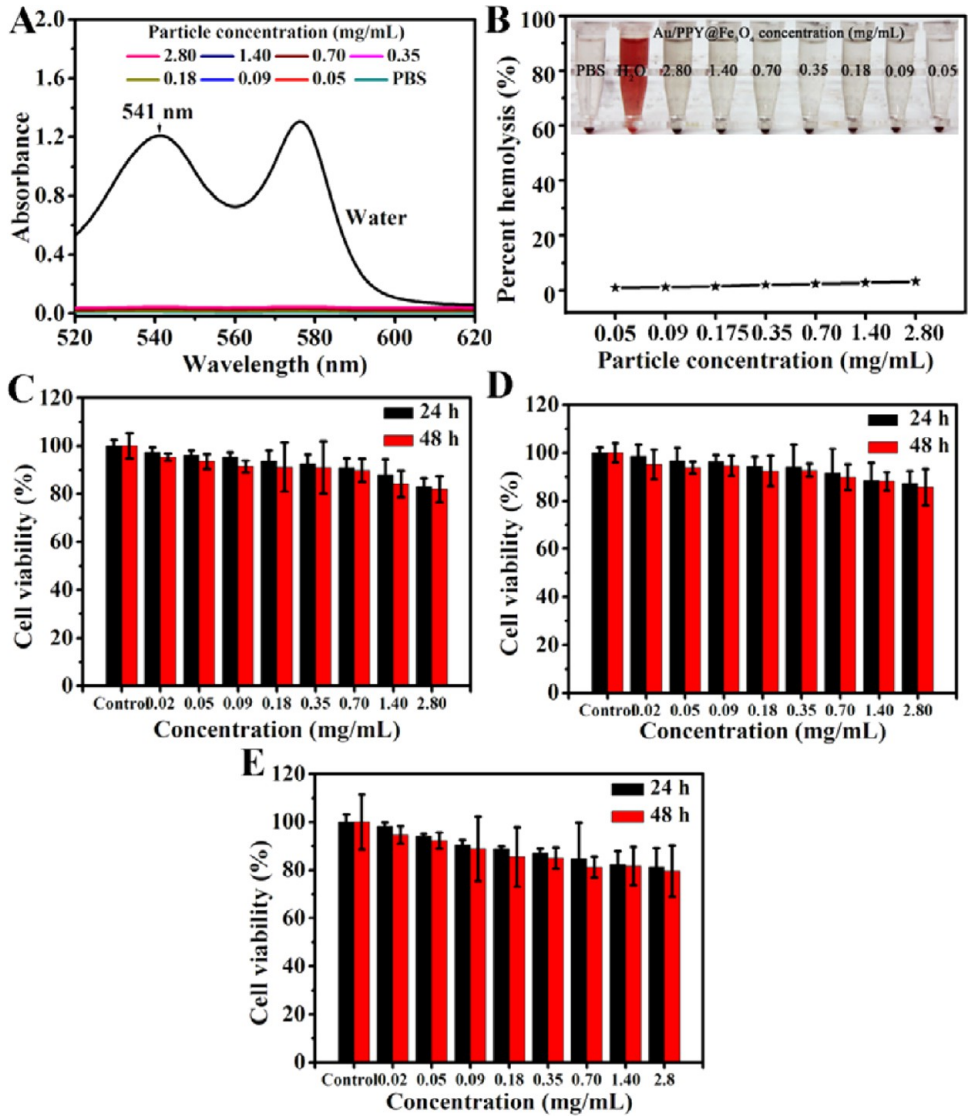

Figure 5. (A) Hemolytic activity of the Au/PPY@Fe_3O_4 nanocomposites at different particle concentrations (0.02, 0.05, 0.09, 0.18, 0.35, 0.7, 1.4, and 2.8 mg/mL, respectively). (B) Hemolytic percent of RBCs incubated with Au/PPY@Fe_3O_4 with different concentrations for 3 h, using deionized water (+) and PBS (−) as positive and negative controls, respectively. Inset: Photographs for direct observation of hemolysis, suggesting that Au/PPY@Fe_3O_4 nanocomposites exhibit good biocompatibility. Viabilities of (C) HeLa cells, (D) L929 cells, and (E) RAW 264.7 cells were estimated by the CCK-8 proliferation method versus incubation concentrations (0.05, 0.09, 0.18, 0.35, 0.7, 1.4, and 2.8 mg/mL) of the solutions of Au/PPY@Fe_3O_4 nanocomposites. Cells were incubated with the solution of Au/PPY@Fe_3O_4 at 37 °C for 24 and 48 h and treated with PBS were used as control.

biocompatibility of the Au/PPY@Fe_3O_4 nanocomposites suggested that they can be potentially used as biocompatible photothermal agents.

3.7. *In Vitro* Photothermal Ablation of HeLa Cells. To investigate the effectiveness of Au/PPY@Fe_3O_4 nanocomposites for cancer therapy by photothermal ablation *in vitro*, HeLa cells cultured in 24-well plates were used as a model. After the HeLa cells were treated with different conditions in parallel, the dead cells differentiated from live ones were stained by using the trypan blue test. It was determined that blue-colored dead cells were only observed after being incubated with 1 mg/mL Au/PPY@Fe_3O_4 nanocomposites and exposed to the NIR 808 nm laser irradiation at 2 W/cm^2 combination treatment for 5 min (Figure 6D). In contrast, there was no apparent change in cell viability, and cell density was discovered when cells were treated with the Au/PPY@Fe_3O_4 (Figure 6B) or laser irradiation (Figure 6C) alone compared with the control (Figure 6A).

3.8. Effect on Cytoskeleton. The actin cytoskeleton, which is a network of fibers composed of proteins, plays a positive role in the maintenance of cellular generation and homeostasis.[78] The cytoskeletal system also has a dynamic structure with distinct forms appropriate for specific tasks, involved in controlling cell adhesion, division, death, and so on.[79] As the main goal of the present study is to evaluate the effectiveness of Au/PPY@Fe_3O_4 nanocomposites for cancer therapy by photothermal ablation, the effect on the actin cytoskeleton was investigated. After variable treatment with Au/PPY@Fe_3O_4 and lasers, green fluorescent staining for the assessment of cytoskeleton was carried out with the Alexa Fluor 488 conjugated phalloidin (Figure 7). As shown in Figure 7, the cells are typically well-spread, display an extensive actin network, and have no apparent change in cell morphology,

DOI: 10.1021/am508837v
ACS Appl. Mater. Interfaces 2015, 7, 4354−4367

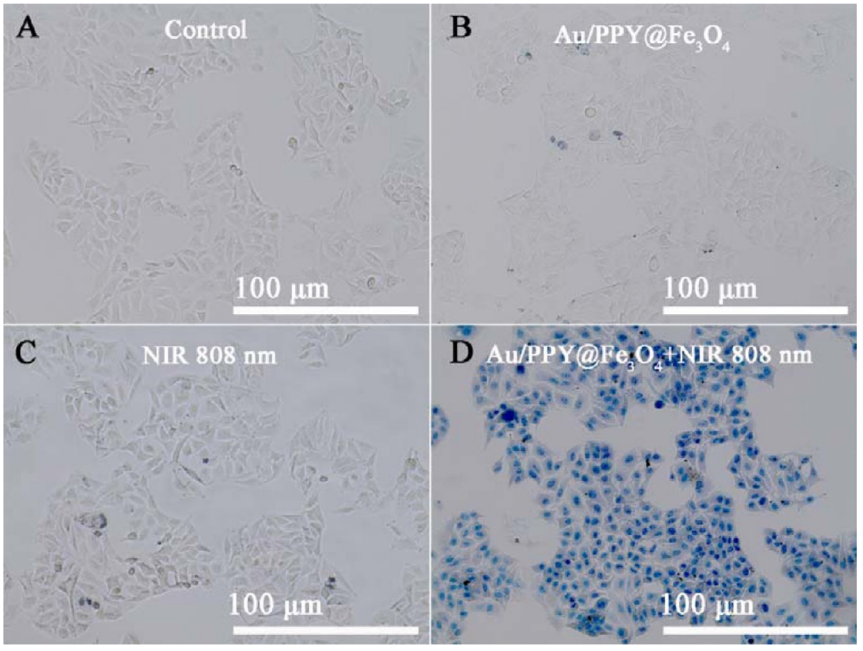

Figure 6. Optical microscopy images of trypan blue stained cells after incubation with different conditions as denoted in each individual image. (A) Neither Au/PPY@Fe_3O_4 nanocomposites nor the NIR-laser applied is used as control. (B) Only Au/PPY@Fe_3O_4 nanocomposites without an NIR 808 laser were used as a treatment with HeLa cells. (C) Only an NIR 808 nm laser (2 W/cm^2, 5 min) without Au/PPY@Fe_3O_4 nanocomposites was used as a treatment with HeLa cells. (D) Au/PPY@Fe_3O_4-treated cells are irradiated by an NIR 808 nm laser with the power density of 2 W/cm^2 for 5 min. Only dead cells can be stained to be blue.

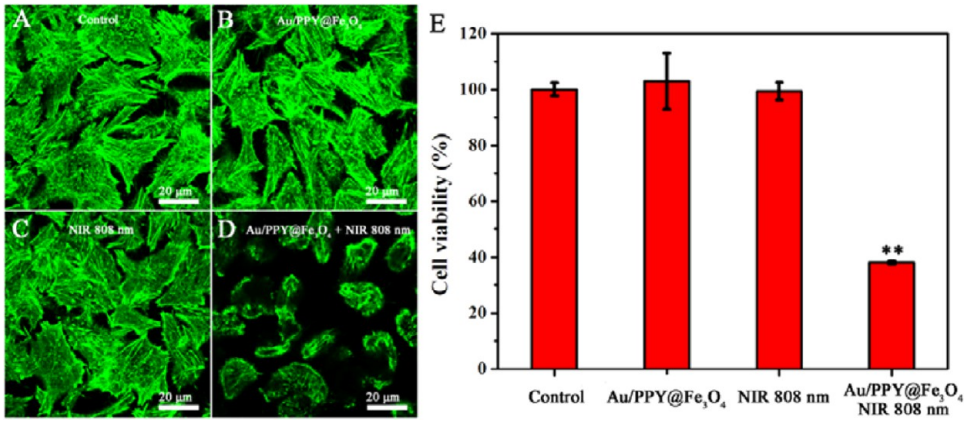

Figure 7. Confocal laser scanning microscopy (CLSM) images of Alexa Fluor 488 conjugated phalloidin (green) stained cells cytoskeleton after incubation with different conditions as denoted in each individual picture. (A) Neither Au/PPY@Fe_3O_4 nanocomposites nor the NIR-laser applied is used as control. (B) Only Au/PPY@Fe_3O_4 nanocomposites without the NIR 808 laser were used as a treatment with HeLa cells. (C) Only the NIR 808 nm laser (2 W/cm^2, 10 min) without Au/PPY@Fe_3O_4 nanocomposites was used as a treatment with HeLa cells. (D) Au/PPY@Fe_3O_4-treated cells are irradiated by the NIR 808 nm laser with the power density of 2 W/cm^2 for 10 min. (E) HeLa cell viability assay of Au/PPY@Fe_3O_4 nanocomposites with different treatment. Data presented as mean ± standard deviation (n = 5), ** p < 0.01.

and density was observed when HeLa cells were treated with Au/PPY@Fe_3O_4 nanocomposites and laser alone compared with the control without nanocomposites and laser (Figure 7A-C). However, HeLa cells treated with Au/PPY@Fe_3O_4 nanocomposites plus an NIR laser experienced clear loss of actin network and substantial cellular death, indicating that Au/PPY@Fe_3O_4 nanocomposites could mediate the photothermal destruction of cytoskeleton architecture (Figure 7D).

The *in vitro* PTA efficiency of the Au/PPY@Fe_3O_4 nanocomposites against HeLa cells was further evaluated by CCK-8 assay. As expected, Figure 7E showed no significant cytotoxicity of the cells treatment with Au/PPY/Fe_3O_4 nanocomposite or irradiation with NIR 808 nm alone. Notably, when simultaneously treated with Au/PPY/Fe_3O_4 nanocomposites under the NIR 808 nm laser irradiation at the power of 2 w/cm^2 for 10 min, significant inhibition of HeLa cell growth was observed, and only less than 40% of HeLa cells remained alive. The results further confirmed the CLSM observation that Au/PPY@Fe_3O_4 nanocomposites could effectively transform the NIR 808 nm laser into heat and thus significantly inhibit the cell proliferation *in vitro*.

3.9. The Integrity of the Lysosomal Membrane. Lysosomes are organelles with an acidic lumen, which were involved in several cellular functions, including repair of the plasma membrane, degradation of macromolecules, antigen presentation, and apoptosis signaling.[80] Lysosomes and

DOI: 10.1021/am508837v
ACS Appl. Mater. Interfaces 2015, 7, 4354−4367

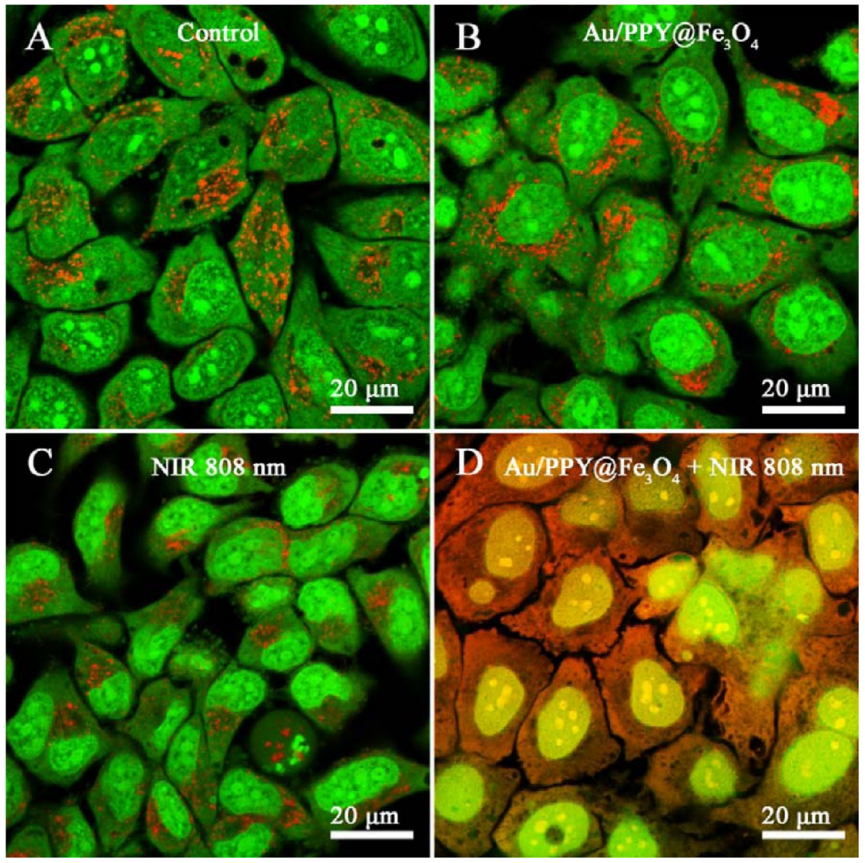

Figure 8. Confocal laser scanning microscopy (CLSM) images of acridine orange (AO) stained cells after incubation with different conditions as denoted in each individual picture. (A) Neither Au/PPY@Fe_3O_4 nanocomposites nor the NIR laser applied is used as control. (B) Only Au/PPY@Fe_3O_4 nanocomposites without the NIR 808 laser were used as a treatment with HeLa cells. (C) Only the NIR 808 nm laser (2 W/cm^2, 5 min) without Au/PPY@Fe_3O_4 nanocomposites was used as a treatment with HeLa cells. (D) Au/PPY@Fe_3O_4-treated cells are irradiated by the NIR 808 nm laser with the power density of 2 W/cm^2 for 5 min.

lysosomal cathepsins have often been linked with cell death.[80] Recent findings have revealed that cell death induced by lysosomal membrane permeabilization (LMP) in cancer cells could play a significant role in cancer and consequently have important therapeutic implications.[80,81] In order to further evaluate the hyperthermic potential of Au/PPY@Fe_3O_4 nanocomposites, LMP of HeLa cell was analyzed using AO staining to determine whether LMP can be changed by laser-converted heat (Figure 8). For the group of Au/PPY@Fe_3O_4-treated cells without irradiation or Au/PPY@Fe_3O_4-untreated cells with laser irradiation, the cellular lysosomes of HeLa cells kept steady, and the cell membrane maintained intact (Figure 8B and C),which was similar to the control group (Figure 8A). However, we observed a decline in red fluorescence of lysosomes and an increase in orange fluorescence of the cytoplasm after combination treatment with Au/PPY@Fe_3O_4 nanocomposites and NIR laser irradiation, indicating a strong disruption in the lysosomal membrane caused the red fluorescence release from the lysosome to the cytosol and led to orange staining throughout the entire cell (Figure 8D). It reveals that the disruption of LMP is possibly attributed to the hyperthermia triggered by the photothermal effect. Furthermore, the lysosomal rupture process is accompanied by hydrolytic enzyme release, which will inevitably lead to acute cancer cell death.[82]

4. CONCLUSION

In summary, uniform Au/PPY@Fe_3O_4 nanocomposites were successfully constructed via a safe and facile method. The synthesized Au/PPY@Fe_3O_4 nanocomposites were used as multifunctional photothermal agents, which exhibit good dispersity, high colloidal stability, strong NIR absorption, superparamagnetic properties, significant photothermal conversion efficiency, photostability, biostability, and low cytotoxicity. Additionally, we demonstrated that these nanocomposites can be used as competent contrast agents for both MRI and CT imaging. Furthermore, the nanocomposites can efficiently kill the cancer cells under the irradiation of an 808 nm laser with a relatively low-power density in a short time. Therefore, we anticipate that the Au/PPY@Fe_3O_4 nanocomposites developed in this study could be used as a multifunctional nanoplatform for cancer therapy, which will implicate increasing opportunities for simultaneous imaging diagnosis and efficient therapy in the biomedical field. More detailed *in vivo* studies of biodistribution and photothermal effect are underway.

■ ASSOCIATED CONTENT

Supporting Information

The FESEM images, size distribution, FTIR spectrum, Raman spectrum, and XPS spectrum and the calculation of photothermal conversion efficiency of Au/PPY@Fe_3O_4 nanocomposites. This material is available free of charge via the Internet at http://pubs.acs.org.

DOI: 10.1021/am508837v
ACS Appl. Mater. Interfaces 2015, 7, 4354−4367

AUTHOR INFORMATION

Corresponding Author

*Phone/Fax: 86 21 6779 2742. E-mail: hcl@dhu.edu.cn.

Notes

The authors declare no competing financial interest.

ACKNOWLEDGMENTS

This work was financially supported by the National Natural Science Foundation of China (31271028), Innovation Program of Shanghai Municipal Education Commission (13ZZ051), Chinese Universities Scientific Fund (CUSF-DH-D-2014035), and Open Foundation of State Key Laboratory for Modification of Chemical Fibers and Polymer Materials (LK1416).

REFERENCES

(1) Peer, D.; Karp, J. M.; Hong, S.; Farokhzad, O. C.; Margalit, R.; Langer, R. Nanocarriers as an Emerging Platform for Cancer Therapy. *Nat. Nanotechnol.* **2007**, *2*, 751−760.

(2) Huang, X. H.; El-Sayed, I. H.; Qian, W.; El-Sayed, M. A. Cancer Cell Imaging and Photothermal Therapy in the Near-Infrared Region by Using Gold Nanorods. *J. Am. Chem. Soc.* **2006**, *128*, 2115−2120.

(3) Zhou, J.; Lu, Z. G.; Zhu, X. J.; Wang, X. J.; Liao, Y.; Ma, Z. F.; Li, F. Y. Nir Photothermal Therapy Using Polyaniline Nanoparticles. *Biomaterials* **2013**, *34*, 9584−9592.

(4) Tian, Q. W.; Jiang, F. R.; Zou, R. J.; Liu, Q.; Chen, Z. G.; Zhu, M. F.; Yang, S. P.; Wang, J. L.; Wang, J. H.; Hu, J. Q. Hydrophilic Cu_9S_5 Nanocrystals: A Photothermal Agent with a 25.7% Heat Conversion Efficiency for Photothermal Ablation of Cancer Cells in Vivo. *ACS Nano* **2011**, *5*, 9761−9771.

(5) Wang, C.; Xu, H.; Liang, C.; Liu, Y. M.; Li, Z. W.; Yang, G. B.; Cheng, H.; Li, Y. G.; Liu, Z. Iron Oxide@Polypyrrole Nanoparticles as a Multifunctional Drug Carrier for Remotely Controlled Cancer Therapy with Synergistic Antitumor Effect. *ACS Nano* **2013**, *7*, 6782−6795.

(6) Boisselier, E.; Astruc, D. Gold Nanoparticles in Nanomedicine: Preparations, Imaging, Diagnostics, Therapies and Toxicity. *Chem. Soc. Rev.* **2009**, *38*, 1759−1782.

(7) Meng, L. J.; Niu, L. Y.; Li, L.; Lu, Q. H.; Fei, Z. F.; Dyson, P. J. Gold Nanoparticles Grown on Ionic Liquid-Functionalized Single-Walled Carbon Nanotubes: New Materials for Photothermal Therapy. *Chem.—Eur. J.* **2012**, *18*, 13314−13319.

(8) Jin, R. C.; Cao, Y. W.; Mirkin, C. A.; Kelly, K. L.; Schatz, G. C.; Zheng, J. G. Photoinduced Conversion of Silver Nanospheres to Nanoprisms. *Science* **2001**, *294*, 1901−1903.

(9) Huang, X. Q.; Tang, S. H.; Mu, X. L.; Dai, Y.; Chen, G. X.; Zhou, Z. Y.; Ruan, F. X.; Yang, Z. L.; Zheng, N. F. Freestanding Palladium Nanosheets with Plasmonic and Catalytic Properties. *Nat. Nanotechnol.* **2011**, *6*, 28−32.

(10) Tang, S. H.; Huang, X. Q.; Zheng, N. F. Silica Coating Improves the Efficacy of Pd Nanosheets for Photothermal Therapy of Cancer Cells Using Near Infrared Laser. *Chem. Commun.* **2011**, *47*, 3948−3950.

(11) Huang, X. Q.; Tang, S. H.; Liu, B. J.; Ren, B.; Zheng, N. F. Enhancing the Photothermal Stability of Plasmonic Metal Nanoplates by a Core-Shell Architecture. *Adv. Mater.* **2011**, *23*, 3420−3425.

(12) Lambert, T. N.; Andrews, N. L.; Gerung, H.; Boyle, T. J.; Oliver, J. M.; Wilson, B. S.; Han, S. M. Water-Soluble Germanium(0) Nanocrystals: Cell Recognition and near-Infrared Photothermal Conversion Properties. *Small* **2007**, *3*, 691−699.

(13) Kam, N. W. S.; O'Connell, M.; Wisdom, J. A.; Dai, H. J. Carbon Nanotubes as Multifunctional Biological Transporters and Near-Infrared Agents for Selective Cancer Cell Destruction. *Proc. Natl. Acad. Sci. U. S. A.* **2005**, *102*, 11600−11605.

(14) Moon, H. K.; Lee, S. H.; Choi, H. C. *In Vivo* Near-Infrared Mediated Tumor Destruction by Photothermal Effect of Carbon Nanotubes. *ACS Nano* **2009**, *3*, 3707−3713.

(15) Wang, X. J.; Wang, C.; Cheng, L.; Lee, S. T.; Liu, Z. Noble Metal Coated Single-Walled Carbon Nanotubes for Applications in Surface Enhanced Raman Scattering Imaging and Photothermal Therapy. *J. Am. Chem. Soc.* **2012**, *134*, 7414−7422.

(16) Meng, L.; Xia, W.; Liu, L.; Niu, L.; Lu, Q. Golden Single-Walled Carbon Nanotubes Prepared Using Double Layer Polysaccharides Bridge for Photothermal Therapy. *ACS Appl. Mater. Interfaces* **2014**, *6*, 4989−4996.

(17) Robinson, J. T.; Tabakman, S. M.; Liang, Y. Y.; Wang, H. L.; Casalongue, H. S.; Vinh, D.; Dai, H. J. Ultrasmall Reduced Graphene Oxide with High Near-Infrared Absorbance for Photothermal Therapy. *J. Am. Chem. Soc.* **2011**, *133*, 6825−6831.

(18) Yang, K.; Zhang, S. A.; Zhang, G. X.; Sun, X. M.; Lee, S. T.; Liu, Z. A. Graphene in Mice: Ultrahigh *in Vivo* Tumor Uptake and Efficient Photothermal Therapy. *Nano Lett.* **2010**, *10*, 3318−3323.

(19) Tian, Q. W.; Tang, M. H.; Sun, Y. G.; Zou, R. J.; Chen, Z. G.; Zhu, M. F.; Yang, S. P.; Wang, J. L.; Wang, J. H.; Hu, J. Q. Hydrophilic Flower-Like CuS Superstructures as an Efficient 980 nm Laser-Driven Photothermal Agent for Ablation of Cancer Cells. *Adv. Mater.* **2011**, *23*, 3542−3547.

(20) Li, Y. B.; Lu, W.; Huang, Q. A.; Huang, M. A.; Li, C.; Chen, W. Copper Sulfide Nanoparticles for Photothermal Ablation of Tumor Cells. *Nanomedicine (London, U. K.)* **2010**, *5*, 1161−1171.

(21) Zhou, M.; Zhang, R.; Huang, M. A.; Lu, W.; Song, S. L.; Melancon, M. P.; Tian, M.; Liang, D.; Li, C. A Chelator-Free Multifunctional [64Cu]CuS Nanoparticle Platform for Simultaneous Micro-PET/CT Imaging and Photothermal Ablation Therapy. *J. Am. Chem. Soc.* **2010**, *132*, 15351−15358.

(22) Hessel, C. M.; Pattani, V. P.; Rasch, M.; Panthani, M. G.; Koo, B.; Tunnell, J. W.; Korgel, B. A. Copper Selenide Nanocrystals for Photothermal Therapy. *Nano Lett.* **2011**, *11*, 2560−2566.

(23) Li, W. H.; Zamani, R.; Gil, P. R.; Pelaz, B.; Ibanez, M.; Cadavid, D.; Shavel, A.; Alvarez-Puebla, R. A.; Parak, W. J.; Arbiol, J.; Cabot, A. Cute Nanocrystals: Shape and Size Control, Plasmonic Properties, and Use as Sers Probes and Photothermal Agents. *J. Am. Chem. Soc.* **2013**, *135*, 7098−7101.

(24) Liu, T.; Wang, C.; Gu, X.; Gong, H.; Cheng, L.; Shi, X. Z.; Feng, L. Z.; Sun, B. Q.; Liu, Z. Drug Delivery with PEGylated MoS_2 Nano-Sheets for Combined Photothermal and Chemotherapy of Cancer. *Adv. Mater.* **2014**, *26*, 3433−3440.

(25) Cheng, L.; Liu, J.; Gu, X.; Gong, H.; Shi, X.; Liu, T.; Wang, C.; Wang, X.; Liu, G.; Xing, H.; Bu, W.; Sun, B.; Liu, Z. PEGylated WS_2 Nanosheets as a Multifunctional Theranostic Agent for in Vivo Dual-Modal CT/Photoacoustic Imaging Guided Photothermal Therapy. *Adv. Mater.* **2014**, *26*, 1886−1893.

(26) Yang, K.; Xu, H.; Cheng, L.; Sun, C. Y.; Wang, J.; Liu, Z. In Vitro and in Vivo Near-Infrared Photothermal Therapy of Cancer Using Polypyrrole Organic Nanoparticles. *Adv. Mater.* **2013**, *25*, 945−945.

(27) Yang, J.; Choi, J.; Bang, D.; Kim, E.; Lim, E. K.; Park, H.; Suh, J. S.; Lee, K.; Yoo, K. H.; Kim, E. K.; Huh, Y. M.; Haam, S. Convertible Organic Nanoparticles for Near-Infrared Photothermal Ablation of Cancer Cells. *Angew. Chem., Int. Ed.* **2011**, *50*, 441−444.

(28) Liu, Y. L.; Ai, K. L.; Liu, J. H.; Deng, M.; He, Y. Y.; Lu, L. H. Dopamine-Melanin Colloidal Nanospheres: An Efficient Near-Infrared Photothermal Therapeutic Agent for *in Vivo* Cancer Therapy. *Adv. Mater.* **2013**, *25*, 1353−1359.

(29) Cheng, L.; Yang, K.; Chen, Q.; Liu, Z. Organic Stealth Nanoparticles for Highly Effective *in Vivo* Near-Infrared Photothermal Therapy of Cancer. *ACS Nano* **2012**, *6*, 5605−5613.

(30) Zha, Z. B.; Yue, X. L.; Ren, Q. S.; Dai, Z. F. Uniform Polypyrrole Nanoparticles with High Photothermal Conversion Efficiency for Photothermal Ablation of Cancer Cells. *Adv. Mater.* **2013**, *25*, 777−782.

(31) Chen, M.; Fang, X. L.; Tang, S. H.; Zheng, N. F. Polypyrrole Nanoparticles for High-Performance *in Vivo* Near-Infrared Photothermal Cancer Therapy. *Chem. Commun.* **2012**, *48*, 8934−8936.

(32) Tian, Q. W.; Wang, Q.; Yao, K. X.; Teng, B. Y.; Zhang, J. Z.; Yang, S. P.; Han, Y. Multifunctional Polypyrrole@Fe_3O_4 Nanoparticles

DOI: 10.1021/am508837v
ACS Appl. Mater. Interfaces 2015, 7, 4354−4367

for Dual-Modal Imaging and in Vivo Photothermal Cancer Therapy. *Small* **2014**, *10*, 1063−1068.
(33) Wang, Q.; Wang, J. D.; Lv, G.; Wang, F.; Zhou, X. K.; Hu, J. Q.; Wang, Q. G. Facile Synthesis of Hydrophilic Polypyrrole Nanoparticles for Photothermal Cancer Therapy. *J. Mater. Sci.* **2014**, *49*, 3484−3490.
(34) Song, X. J.; Gong, H.; Yin, S. N.; Cheng, L.; Wang, C.; Li, Z. W.; Li, Y. G.; Wang, X. Y.; Liu, G.; Liu, Z. Ultra-Small Iron Oxide Doped Polypyrrole Nanoparticles for *in Vivo* Multimodal Imaging Guided Photothermal Therapy. *Adv. Funct. Mater.* **2014**, *24*, 1194−1201.
(35) He, C. L.; Nie, W.; Feng, W. Engineering of Biomimetic Nanofibrous Matrices for Drug Delivery and Tissue Engineering. *J. Mater. Chem. B* **2014**, *2*, 7828−7848.
(36) Thompson, B. C.; Moulton, S. E.; Ding, J.; Richardson, R.; Cameron, A.; O'Leary, S.; Wallace, G. G.; Clark, G. M. Optimising the Incorporation and Release of a Neurotrophic Factor Using Conducting Polypyrrole. *J. Controlled Release* **2006**, *116*, 285−294.
(37) Vaitkuviene, A.; Kaseta, V.; Voronovic, J.; Ramanauskaite, G.; Biziuleviciene, G.; Ramanaviciene, A.; Ramanavicius, A. Evaluation of Cytotoxicity of Polypyrrole Nanoparticles Synthesized by Oxidative Polymerization. *J. Hazard. Mater.* **2013**, *250*, 167−174.
(38) Stewart, E. M.; Liu, X.; Clark, G. M.; Kapsa, R. M. I.; Wallace, G. G. Inhibition of Smooth Muscle Cell Adhesion and Proliferation on Heparin-Doped Polypyrrole. *Acta Biomater.* **2012**, *8*, 194−200.
(39) Ramanaviciene, A.; Kausaite, A.; Tautkus, S.; Ramanavicius, A. Biocompatibility of Polypyrrole Particles: An *in Vivo* Study in Mice. *J. Pharm. Pharmacol.* **2007**, *59*, 311−315.
(40) Jin, Y. D.; Jia, C. X.; Huang, S. W.; O'Donnell, M.; Gao, X. H. Multifunctional Nanoparticles as Coupled Contrast Agents. *Nat. Commun.* **2010**, *1*, 41.
(41) Liu, J. H.; Han, J. G.; Kang, Z. C.; Golamaully, R.; Xu, N. N.; Li, H. P.; Han, X. L. In Vivo Near-Infrared Photothermal Therapy and Computed Tomography Imaging of Cancer Cells Using Novel Tungsten-Based Theranostic Probe. *Nanoscale* **2014**, *6*, 5770−5776.
(42) Zhang, X.; Xu, X. W.; Li, T. T.; Lin, M.; Lin, X. Y.; Zhang, H.; Sun, H. C.; Yang, B. Composite Photothermal Platform of Polypyrrole-Enveloped Fe_3O_4 Nanoparticle Self-Assembled Superstructures. *ACS Appl. Mater. Interfaces* **2014**, *6*, 14552−14561.
(43) Zha, Z. B.; Wang, J. R.; Zhang, S. H.; Wang, S. M.; Qu, E.; Zhang, Y. Y.; Dai, Z. F. Engineering of Perfluorooctylbromide Polypyrrole Nano-/Microcapsules for Simultaneous Contrast Enhanced Ultrasound Imaging and Photothermal Treatment of Cancer. *Biomaterials* **2014**, *35*, 287−293.
(44) Lee, T.; Bang, D.; Park, Y.; Kim, S. H.; Choi, J.; Park, J.; Kim, D.; Kim, E.; Suh, J. S.; Huh, Y. M.; Haam, S. Gadolinium-Enriched Polyaniline Particles (Gpaps) for Simultaneous Diagnostic Imaging and Localized Photothermal Therapy of Epithelial Cancer. *Adv. Healthcare Mater.* **2014**, *3*, 1408−1414.
(45) Jin, Y. S.; Li, Y. Y.; Ma, X. B.; Zha, Z. B.; Shi, L. L.; Tian, J.; Dai, Z. F. Encapsulating Tantalum Oxide into Polypyrrole Nanoparticles for X-Ray CT/Photoacoustic Bimodal Imaging-Guided Photothermal Ablation of Cancer. *Biomaterials* **2014**, *35*, 5795−5804.
(46) Dong, W. J.; Li, Y. S.; Niu, D. C.; Ma, Z.; Liu, X. H.; Gu, J. L.; Zhao, W. R.; Zheng, Y. Y.; Shi, J. L. A Simple Route to Prepare Monodisperse Au NP-Decorated, Dye-Doped, Superparamagnetic Nanocomposites for Optical, MR, and CT Trimodal Imaging. *Small* **2013**, *9*, 2500−2508.
(47) Chuang, Y. C.; Lin, C. J.; Lo, S. F.; Wang, J. L.; Tzou, S. C.; Yuan, S. S.; Wang, Y. M. Dual Functional AuNRs@MnMEIOs Nanoclusters for Magnetic Resonance Imaging and Photothermal Therapy. *Biomaterials* **2014**, *35*, 4678−4687.
(48) Lu, W. T.; Singh, A. K.; Khan, S. A.; Senapati, D.; Yu, H. T.; Ray, P. C. Gold Nano-Popcorn-Based Targeted Diagnosis, Nanotherapy Treatment, and *in Situ* Monitoring of Photothermal Therapy Response of Prostate Cancer Cells Using Surface-Enhanced Raman Spectroscopy. *J. Am. Chem. Soc.* **2010**, *132*, 18103−18114.
(49) Koo, H.; Huh, M. S.; Sun, I. C.; Yuk, S. H.; Choi, K.; Kim, K.; Kwon, I. C. *In Vivo* Targeted Delivery of Nanoparticles for Theranosis. *Acc. Chem. Res.* **2011**, *44*, 1018−1028.
(50) Xie, J.; Liu, G.; Eden, H. S.; Ai, H.; Chen, X. Y. Surface-Engineered Magnetic Nanoparticle Platforms for Cancer Imaging and Therapy. *Acc. Chem. Res.* **2011**, *44*, 883−892.
(51) Wang, S. T.; Chen, K. J.; Wu, T. H.; Wang, H.; Lin, W. Y.; Ohashi, M.; Chiou, P. Y.; Tseng, H. R. Photothermal Effects of Supramolecularly Assembled Gold Nanoparticles for the Targeted Treatment of Cancer Cells. *Angew. Chem., Int. Ed.* **2010**, *49*, 3777−3781.
(52) Jain, P. K.; El-Sayed, I. H.; El-Sayed, M. A. Au Nanoparticles Target Cancer. *Nano Today* **2007**, *2*, 18−29.
(53) Dong, W. J.; Li, Y. S.; Niu, D. C.; Ma, Z.; Gu, J. L.; Chen, Y.; Zhao, W. R.; Liu, X. H.; Liu, C. S.; Shi, J. L. Facile Synthesis of Monodisperse Superparamagnetic Fe_3O_4 Core@Hybrid@Au Shell Nanocomposite for Bimodal Imaging and Photothermal Therapy. *Adv. Mater.* **2011**, *23*, 5392−5397.
(54) Li, J.; Han, J. S.; Xu, T. S.; Guo, C. R.; Bu, X. Y.; Zhang, H.; Wang, L. P.; Sun, H. C.; Yang, B. Coating Urchinlike Gold Nanoparticles with Polypyrrole Thin Shells to Produce Photothermal Agents with High Stability and Photothermal Transduction Efficiency. *Langmuir* **2013**, *29*, 7102−7110.
(55) Gorelikov, I.; Matsuura, N. Single-Step Coating of Mesoporous Silica on Cetyltrimethyl Ammonium Bromide-Capped Nanoparticles. *Nano Lett.* **2008**, *8*, 369−373.
(56) Wang, L. M.; Liu, Y.; Li, W.; Jiang, X. M.; Ji, Y. L.; Wu, X. C.; Xu, L. G.; Qiu, Y.; Zhao, K.; Wei, T. T.; Li, Y. F.; Zhao, Y. L.; Chen, C. Y. Selective Targeting of Gold Nanorods at the Mitochondria of Cancer Cells: Implications for Cancer Therapy. *Nano Lett.* **2011**, *11*, 772−780.
(57) Roper, D. K.; Ahn, W.; Hoepfner, M. Microscale Heat Transfer Transduced by Surface Plasmon Resonant Gold Nanoparticles. *J. Phys. Chem. C* **2007**, *111*, 3636−3641.
(58) Feng, W.; Zhou, X. J.; He, C. L.; Qiu, K. X.; Nie, W.; Chen, L.; Wang, H. S.; Mo, X. M.; Zhang, Y. Z. Polyelectrolyte Multilayer Functionalized Mesoporous Silica Nanoparticles for pH-Responsive Drug Delivery: Layer Thickness-Dependent Release Profiles and Biocompatibility. *J. Mater. Chem. B* **2013**, *1*, 5886−5898.
(59) Feng, W.; Nie, W.; He, C. L.; Zhou, X. J.; Chen, L.; Qiu, K. X.; Wang, W. Z.; Yin, Z. Q. Effect of pH-Responsive Alginate/Chitosan Multilayers Coating on Delivery Efficiency, Cellular Uptake and Biodistribution of Mesoporous Silica Nanoparticles Based Nanocarriers. *ACS Appl. Mater. Interfaces* **2014**, *6*, 8447−8460.
(60) Hong, J. Y.; Yoon, H.; Jang, J. Kinetic Study of the Formation of Polypyrrole Nanoparticles in Water-Soluble Polymer/Metal Cation Systems: A Light-Scattering Analysis. *Small* **2010**, *6*, 679−686.
(61) Shen, L. F.; Laibinis, P. E.; Hatton, T. A. Bilayer Surfactant Stabilized Magnetic Fluids: Synthesis and Interactions at Interfaces. *Langmuir* **1999**, *15*, 447−453.
(62) Shao, D.; Xia, A.; Hu, J. H.; Wang, C. C.; Yu, W. M. Monodispersed Magnetite/Silica Composite Microspheres: Preparation and Application for Plasmid DNA Purification. *Colloids Surf., A* **2008**, *322*, 61−65.
(63) Abdulla, H. S.; Abbo, A. I. Optical and Electrical Properties of Thin Films of Polyaniline and Polypyrrole. *Int. J. Electrochem. Sci.* **2012**, *7*, 10666−10678.
(64) Zhang, J. L.; Srivastava, R. S.; Misra, R. D. K. Core-Shell Magnetite Nanoparticles Surface Encapsulated with Smart Stimuli-Responsive Polymer: Synthesis, Characterization, and LCST of Viable Drug-Targeting Delivery System. *Langmuir* **2007**, *23*, 6342−6351.
(65) Kurchania, R.; Sawant, S. S.; Ball, R. J. Synthesis and Characterization of Magnetite/Polyvinyl Alcohol Core-Shell Composite Nanoparticles. *J. Am. Ceram. Soc.* **2014**, *97*, 3208−3215.
(66) Sahoo, S.; Dhibar, S.; Hatui, G.; Bhattacharya, P.; Das, C. K. Graphene/Polypyrrole Nanofiber Nanocomposite as Electrode Material for Electrochemical Supercapacitor. *Polymer* **2013**, *54*, 1033−1042.
(67) Tian, B.; Zerbi, G. Lattice-Dynamics and Vibrational-Spectra of Polypyrrole. *J. Chem. Phys.* **1990**, *92*, 3886−3891.
(68) Lopez-Garcia, F.; Canche-Escamilla, G.; Ocampo-Flores, A. L.; Roquero-Tejeda, P.; Ordonez, L. C. Controlled Size Nano-Polypyrrole

DOI: 10.1021/am508837v
ACS Appl. Mater. Interfaces 2015, 7, 4354−4367

Synthetized in Micro-Emulsions as Pt Support for the Ethanol Electro-Oxidation Reaction. *Int. J. Electrochem. Sci.* **2013**, *8*, 3794−3813.
(69) Jiwei, L.; Jingxia, Q.; Miao, Y. Q.; Chen, J. R. Preparation and Characterization of Pt-Polypyrrole Nanocomposite for Electrochemical Reduction of Oxygen. *J. Mater. Sci.* **2008**, *43*, 6285−6288.
(70) Vishnuvardhan, T. K.; Kulkarni, V. R.; Basavaraja, C.; Raghavendra, S. C. Synthesis, Characterization and A.C. Conductivity of Polypyrrole/Y_2O_3 Composites. *Bull. Mater. Sci.* **2006**, *29*, 77−83.
(71) Mezni, A.; Balti, I.; Mlayah, A.; Jouini, N.; Smiri, L. S. Hybrid Au-Fe_3O_4 Nanoparticles: Plasmonic, Surface Enhanced Raman Scattering, and Phase Transition Properties. *J. Phys. Chem. C* **2013**, *117*, 16166−16174.
(72) Chen, Y. J.; Xiao, G.; Wang, T. S.; Ouyang, Q. Y.; Qi, L. H.; Ma, Y.; Gao, P.; Zhu, C. L.; Cao, M. S.; Jin, H. B. Porous Fe_3O_4/Carbon Core/Shell Nanorods: Synthesis and Electromagnetic Properties. *J. Phys. Chem. C* **2011**, *115*, 13603−13608.
(73) Tiwari, S.; Prakash, R.; Choudhary, R. J.; Phase, D. M. Oriented Growth of Fe_3O_4 Thin Film on Crystalline and Amorphous Substrates by Pulsed Laser Deposition. *J. Phys. D: Appl. Phys.* **2007**, *40*, 4943−4947.
(74) Xi, G. C.; Wang, C.; Wang, X. The Oriented Self-Assembly of Magnetic Fe_3O_4 Nanoparticles into Monodisperse Microspheres and Their Use as Substrates in the Formation of Fe_3O_4 Nanorods. *Eur. J. Inorg. Chem.* **2008**, 425−431.
(75) Wang, L. Y.; Bai, J. W.; Li, Y. J.; Huang, Y. Multifunctional Nanoparticles Displaying Magnetization and Near-IR Absorption. *Angew. Chem., Int. Ed.* **2008**, *47*, 2439−2442.
(76) Tian, Q. W.; Hu, J. Q.; Zhu, Y. H.; Zou, R. J.; Chen, Z. G.; Yang, S. P.; Li, R. W.; Su, Q. Q.; Han, Y.; Liu, X. G. Sub-10 nm Fe_3O_4@$Cu_{2-X}S$ Core-Shell Nanoparticles for Dual-Modal Imaging and Photothermal Therapy. *J. Am. Chem. Soc.* **2013**, *135*, 8571−8577.
(77) Cai, H. D.; Li, K. G.; Shen, M. W.; Wen, S. H.; Luo, Y.; Peng, C.; Zhang, G. X.; Shi, X. Y. Facile Assembly of Fe_3O_4@Au Nanocomposite Particles for Dual Mode Magnetic Resonance and Computed Tomography Imaging Applications. *J. Mater. Chem.* **2012**, *22*, 15110−15120.
(78) Gourlay, C. W.; Ayscough, K. R. The Actin Cytoskeleton: A Key Regulator of Apoptosis and Ageing? *Nat. Rev. Mol. Cell Biol.* **2005**, *6*, 583−585.
(79) Rangel, M.; Prado, M. P.; Konno, K.; Naoki, H.; Freitas, J. C.; Machado-Santelli, G. M. Cytoskeleton Alterations Induced by Geodia Corticostylifera Depsipeptides in Breast Cancer Cells. *Peptides* **2006**, *27*, 2047−2057.
(80) Appelqvist, H.; Sandin, L.; Bjornstrom, K.; Saftig, P.; Garner, B.; Ollinger, K.; Kagedal, K. Sensitivity to Lysosome-Dependent Cell Death is Directly Regulated by Lysosomal Cholesterol Content. *PLoS One* **2012**, *7*, e50262.
(81) Gyparaki, M. T.; Papavassiliou, A. G. Lysosome: The Cell's 'Suicidal Bag' as a Promising Cancer Target. *Trends Mol. Med.* **2014**, *20*, 239−241.
(82) Liu, Z. M.; Xiao, Y.; Chen, W.; Wang, Y.; Wang, B.; Wang, G. C.; Xu, X. R.; Tang, R. K. Calcium Phosphate Nanoparticles Primarily Induce Cell Necrosis through Lysosomal Rupture: The Origination of Material Cytotoxicity. *J. Mater. Chem. B* **2014**, *2*, 3480−3489.

DOI: 10.1021/am508837v
ACS Appl. Mater. Interfaces 2015, 7, 4354−4367